A Spatio-Temporal Hypergraph Forecasting Model for Transportation Revitalization Index Following the COVID-19 Pandemic

Zhiqiang Lv[1,2], Jianbo Li[1*], Zhihao Xu[1], Rongkun Ye[1],
[1] College of Computer Science & Technology, Qingdao University, Qingdao, 266071, China
[2] Institute of Computing Technology, Chinese Academy of Sciences, Beijing, 100190, China

Abstract
The COVID-19 pandemic has precipitated a profound shock to socio-economic systems across the globe, with its impact most conspicuously manifested in the transportation sector. One substantial gauge of municipal transportation recovery post-pandemic is the urban Transportation Revitalization Index (TRI). Predictive research on TRI serves as a pivotal tool for assessing the recuperation of city transport and economic navigation and for settling on pertinent policy-making decisions. Despite the prevalence of spatio-temporal forecasting models built upon graph theory in existing research, these models encounter limitations when tackling intricate interactions across multiple city nodes. The descriptive scope of these models is confined to pairwise connected nodes, failing to capture high-dimensional characteristics and latent non-linear attributes. In an endeavor to rectify this flaw, this study introduces hypergraphs as an alternative to traditional graph models, resulting in the formulation of a spatio-temporal hypergraph forecasting model. A single edge in a hypergraph intuitively portrays complex spatial connections among multiple cities since it can link numerous nodes. Thus, a hypergraph convolution module is constructed to decipher and learn the high-dimensional spatial relationship attributes between cities. Residual modules based on dilated and causal convolutions are established to study the long-term dependency properties of fluctuations in the TRI, structuring a temporal convolution module via multi-layered residual connections. As the data corresponding to the TRI is intertwined with the development of the pandemic, a data fusion module is assembled to bring about dynamic blending of data on the TRI and COVID-19. By comparing experimental results on real-world data with the baseline model set up in this study, the model proposed in this study demonstrates superior performance, with a comprehensive error reduction of 51.66%.

Keywords: COVID-19, spatio-temporal model, transportation revitalization index, hypergraph.

1 Introduction

1.1 Profound Impact of COVID-19 on Transportation System

The COVID-19 pandemic has engendered profound transformations within the transportation infrastructure of China [1]. In the shadow of the pandemic, prophylactic measures aimed at curtailing the spread of the virus, including city-specific lockdown policies and travel constraints, instigated a dramatic plummet in the requisition of public and long-haul transportation. This severe contraction has wielded direct impact upon a variety of conveyances, ranging from buses, subways, and taxis to airline services and train operations. In addition, the pandemic has served as a crucible for reshaping the structure of freight industry demands, thereby yielding an intricate scenario. Whilst demands for certain sectors have succumbed to decline, others, particularly those associated with the transport of key commodities like medical apparatus and food supplies [2], have witnessed an inflated necessity. On a parallel context, apprehension of viral exposure within shared transport spaces has provoked a shift in the requisition of private transportation modes [3]. An intensification is, thus, observed in the usage of privately-owned vehicles, rental services, as well as pedal and electric skateboards [4]. Both present and future

*Jianbo Li is the corresponding author. E-mail: lijianbo@ubinet.cn.

perspectives suggest that the pandemic may serve as a catalyst for propelling the trends of remote working and learning modalities—subsequently morphing commuting necessities and ushering in an increased acceptance of eco-conscious travel methods. In essence, the protruding echoes of the COVID-19 pandemic transcend instantaneous effects [5] on the transportation infrastructure of China, potentially wielding lasting consequences on the future contours of transportation planning and travel modus operandi.

Leveraging the copious mobility data procured from the Didi Dache platform, an opportunity is presented to compute an average value for the index referred to as Travel Time Index (TTI) [6], providing a concise assessment of traffic conditions within the major cities across the national expanse in the first quarter (Q1) of the year 2020. Explicitly defined, the TTI represents a quotient of the actual travel time over the estimated travel duration under conditions of unconstrained flow [7]. This metric invariably assumes paramount significance as an effective barometer of municipal traffic conditions: elevation in TTI values is indicative of the exacerbation of traffic congestion. Specifically, a TTI equivalent to 1 suggests traffic conditions exist in an ideal bandwidth, signifying that actual travel time aligns with the estimated duration under conditions of free flow. In contrast, a TTI transcending the value of 1 illustrates that the actual travel duration extends beyond the time estimated under unconstrained flow conditions. If the TTI inflates significantly above 1, the city could be grappling with grave congestion issues. Hence, under the umbrella of the given theoretical framework, buttressed with data drawn from Didi Dache platform [8], comprehensive insights into the traffic conditions across China's major cities during the Q1 of 2020 can be accurately solicited.

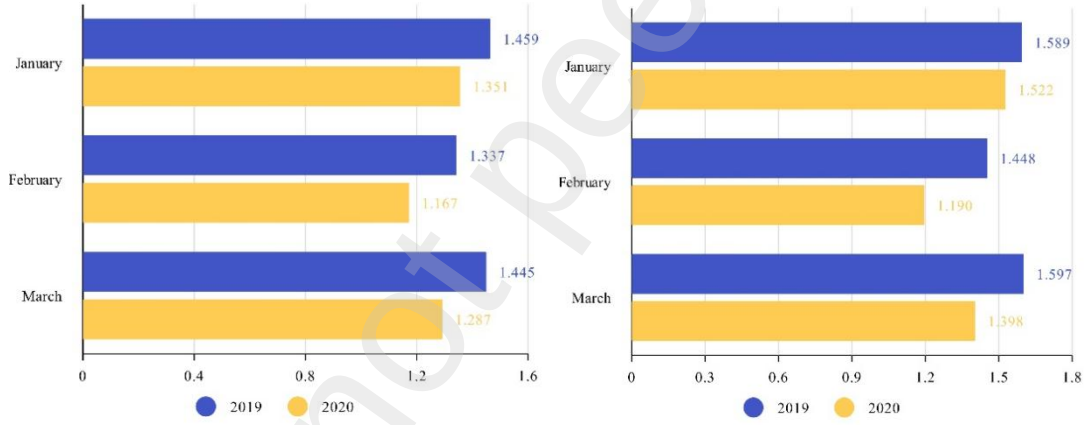

(a) (b)

Figure 1. Alterations in Whole-day TTI (a) and Peak TTI during Workdays (b) in Key Chinese Cities during the Q1 of 2020.

In the Q1 of 2020, the whole-day TTI of key Chinese cities bore witness to a fluctuating trend painting a picture of initial decline followed by eventual increment, as demonstrated in Figure 1(a). In comparison to the opening quarter of 2019, various extents of diminutions in the monthly whole-day TTI of notable Chinese cities were discernible during the first trimester of 2020. This phenomenon has been attributed to the repercussions of the COVID-19 outbreak along with the corresponding preventative quarantine measures implemented at diverse locales. Evidently, this echoes the immediate bearing of pandemic conditions on mobility, not to mention the role containment policies have played in assuaging the viral spread [9]. During the Q1 of 2020, the TTI during the morning and evening peak hours of workdays in these prominent cities initially depicted a decrement, followed by a gradual ascend, as a direct consequence of the novel COVID-19 pandemic, as exhibited in Figure 1(b). In February, a seismic dip in the TTI metrics during peak traffic hours was observed, attributed to the confluence of the Chinese Lunar New Year holiday period and the epidemic incidence. Upon juxtaposing with the corresponding window from the preceding year, the TTI indices of the major Chinese cities in the initial three months

of 2020 showcased a downward trajectory when compared with the analogous period of 2019. In particular, February served witness to the most drastic plummet. This unequivocally corroborates the substantial impacts of the intense outbreak crisis on transportation conditions during this epoch [10].

Table 1. City Ranking of Whole-Day TTI in Q1 of 2020 in China

Rank	City	TTI	QoQ Change in TTI	YoY Change in TTI	Average Speed (km/h)	QoQ Change in Speed	YoY Change in Speed
1	Yinchuan	1.359	-3.17%	-4.75%	43.415	14.56%	13.83%
2	Xi'an	1.345	-13.20%	-15.14%	41.945	27.32%	24.94%
3	Chengdu	1.328	-11.26%	-10.44%	41.613	17.35%	10.41%
4	Shenyang	1.327	-11.52%	-10.17%	39.141	9.68%	6.64%
5	Xining	1.318	-9.72%	-12.85%	37.898	6.91%	12.49%
6	Shanghai	1.313	-13.67%	-7.37%	41.752	18.14%	5.98%
7	Nanjing	1.311	-8.23%	-8.58%	43.711	13.27%	7.79%
8	Jinan	1.307	-9.57%	-9.96%	47.427	12.82%	12.42%
9	Chongqing	1.303	-15.96%	-15.32%	45.072	25.77%	17.17%
10	Dalian	1.301	-11.37%	-9.03%	38.175	11.84%	8.85%
11	Zhengzhou	1.301	-9.10%	-14.23%	46.505	13.84%	16.78%
12	Wenzhou	1.299	-10.61%	-10.20%	42.121	18.31%	10.86%
13	Kunming	1.299	-10.55%	-9.19%	41.429	16.72%	9.13%
14	Lanzhou	1.297	-7.46%	-9.45%	46.315	5.24%	7.50%
15	Shijiazhuang	1.296	-9.44%	-10.67%	45.846	12.93%	9.90%
16	Guiyang	1.292	-15.09%	-11.15%	43.569	16.34%	3.48%
17	Suzhou	1.291	-5.16%	-3.35%	47.577	10.21%	2.46%
18	Changchun	1.289	-23.54%	-14.64%	38.150	21.71%	6.64%
19	Hangzhou	1.285	-12.03%	-10.02%	42.691	19.24%	10.02%
20	Hohhot	1.282	-16.27%	-15.37%	39.089	13.77%	8.07%
21	Harbin	1.280	-23.12%	-16.45%	39.211	22.65%	10.71%
22	Taiyuan	1.280	-9.25%	-12.00%	43.171	13.66%	11.54%
23	Yantai	1.280	-4.25%	-4.75%	45.718	-0.67%	1.98%
24	Wuxi	1.279	-6.75%	-5.45%	48.766	10.28%	4.19%
25	Xuzhou	1.279	-6.69%	-8.58%	48.362	12.94%	8.76%
26	Shenzhen	1.273	-14.68%	-9.93%	41.791	22.00%	9.63%
27	Qingdao	1.271	-10.06%	-7.49%	42.806	10.97%	5.90%
28	Guangzhou	1.268	-15.48%	-10.52%	44.765	23.81%	7.77%
29	Fuzhou	1.265	-8.74%	-11.81%	45.252	15.63%	13.50%
30	Jiaxing	1.259	-5.63%	-1.86%	56.367	13.14%	2.09%
31	Hefei	1.257	-10.26%	-11.98%	44.686	17.23%	12.04%
32	Jinhua	1.257	-8.43%	-7.76%	46.148	17.16%	6.33%
33	Beijing	1.257	-20.50%	-17.54%	42.666	28.13%	19.62%
34	Taizhou	1.256	-9.87%	-9.81%	49.881	23.45%	17.70%
35	Changsha	1.254	-12.58%	-13.01%	43.779	18.85%	15.43%
36	Nanchang	1.253	-8.97%	-11.78%	43.717	15.72%	13.51%
37	Shaoxing	1.252	-6.86%	-4.45%	52.207	13.71%	1.65%
38	Ningbo	1.252	-8.36%	-8.10%	47.224	11.86%	5.14%
39	Urumqi	1.249	-18.56%	-15.64%	48.455	37.19%	29.52%
40	Nantong	1.243	-5.41%	-7.50%	57.307	13.30%	13.46%

41	Xiamen	1.243	-11.26%	-10.46%	42.589	16.17%	11.76%
42	Zhuhai	1.239	-12.65%	-9.95%	46.148	17.05%	8.96%
43	Zhongshan	1.236	-11.32%	-7.74%	48.232	18.70%	4.66%
44	Changzhou	1.234	-4.38%	-5.95%	52.745	10.34%	5.88%
45	Dongguan	1.234	-14.19%	-10.08%	46.088	24.39%	9.32%
46	Nanning	1.227	-9.92%	-12.97%	46.740	17.58%	15.72%
47	Tianjin	1.222	-10.66%	-8.34%	44.823	8.08%	0.97%
48	Haikou	1.221	-11.29%	-12.11%	45.727	22.67%	18.20%
49	Huizhou	1.216	-9.20%	-7.01%	54.081	19.30%	5.90%
50	Foshan	1.215	-13.30%	-9.24%	50.190	21.49%	8.93%

In an analysis predicated on data from Q1 of 2020, the TTI for key Chinese cities were meticulously calculated and then juxtaposed with comparative data spanning both Q1 and Q4 of 2019. The conditions of vehicular flow during this specific period were chiefly shaped by a combination of variables, as illustrated in Table 1, including the Lunar New Year holiday, the COVID-19 pandemic, and the roll-out of related preventative health measures across various locales. Upon the emergence and subsequent encroachment of COVID-19, a profound and lingering impact on the transportation systems within Chinese urban sprawl becomes palpably evident, heralding noticeable variations in standard operation [11]. Notably, Yinchuan city demonstrated limited influence with a whole-day TTI of 1.359, securing the city's position as experiencing the most profound traffic congestion nationwide. Following the severity of traffic congestion, a decathlon of urban areas hosted the most critical congestion issues, in descending order: Yinchuan, Xi'an, Chengdu, Shenyang, Xining, Shanghai, Nanjing, Jinan, Chongqing, and Dalian. Within the list of top 50 cities for traffic congestion throughout Q1 of 2020, a universally downward trend manifest across all their TTIs. Traffic in several cities, such as Changchun, Harbin, and Beijing, exhibited particularly significant declines [12]. When contrasted with Q1 of 2019, a generally diminishing TTI trend for the top 50 most congested cities was likewise noticeable, with Beijing, Harbin, and Urumqi leading the steepest descents. These shifts underscore the profound impact of the COVID-19 pandemic on urban transportation within China.

1.2 Analysis of Transportation Revitalization Index

As the grip of the COVID-19 pandemic progressively relaxes, a systematic and orderly resumption of work and production in enterprises has been initiated [13]. Amidst the gradual restoration of urban regularities, transportation assumes a foundational role, wherein road conditions and travel data essentially mirror the recuperation status of urban productivity and consumer activities. This discourse is particularly intrigued by the temporal changes in what we refer to as the Transportation Revitalization Index (TRI) [14], a tool that skillfully unveils the current circumstances pertinent to resuming work and production in cities. The TRI principally relies upon a vast continuum of trajectory data from the Didi Dache platform, alongside other travel information such as the TTI. By employing methods such as data fitting, cross-validation, and weighted treatment, Didi Dache platform constructed an index that scientifically and objectively echoes the activity level of urban transportation. Furthermore, trends in the index reveal shifts in urban transportation activity, indirectly reflecting the revival tendencies of the cities.

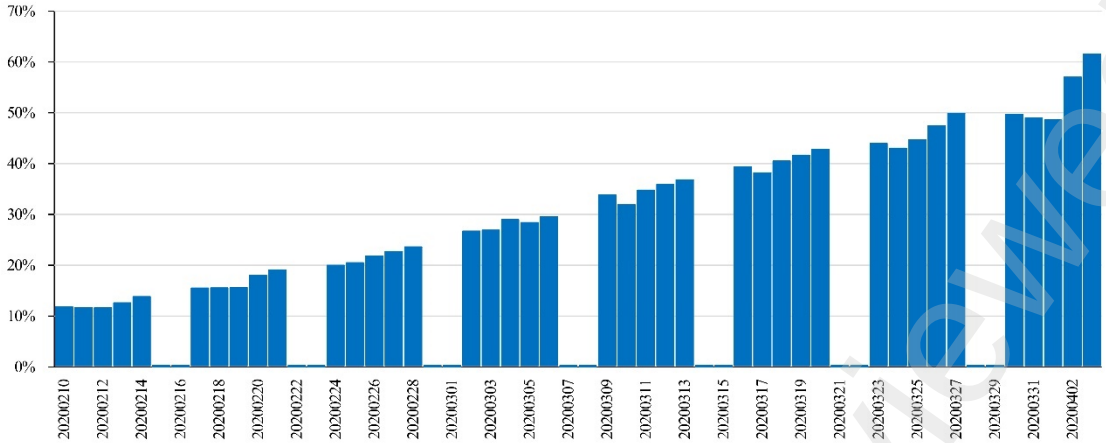

Figure 2. Daily Variations in the TRI for Chinese Cities in the Q1 of 2020.

Since February 10, 2020, our observations indicate a steady upswing in the TRI across Chinese cities, as shown in Figure 2. This phenomenon correlates closely with the reinstatement of work in numerous locations following February 10, and the effective implementation of pandemic prevention measures. Ensured by reliable prevention strategies, the situation unfolded favorably and the gradual recovery of urban transport vitality was a logical consequence [15]. Particularly, the TRI stood at 11.79% on February 10. Merely within a month, by the conclusion of February, the index had mushroomed to 25.55%. Remarkably, as we navigated towards the end of the first quarter, on April 3, the index demonstrated a nearly 50 percentile point surge in comparison with February 10, reaching 61.54%. Accordingly, the evolution of the TRI permits a reasonable deduction: the vitality of transportation across Chinese cities generally rebounded to more than 60% of regular levels.

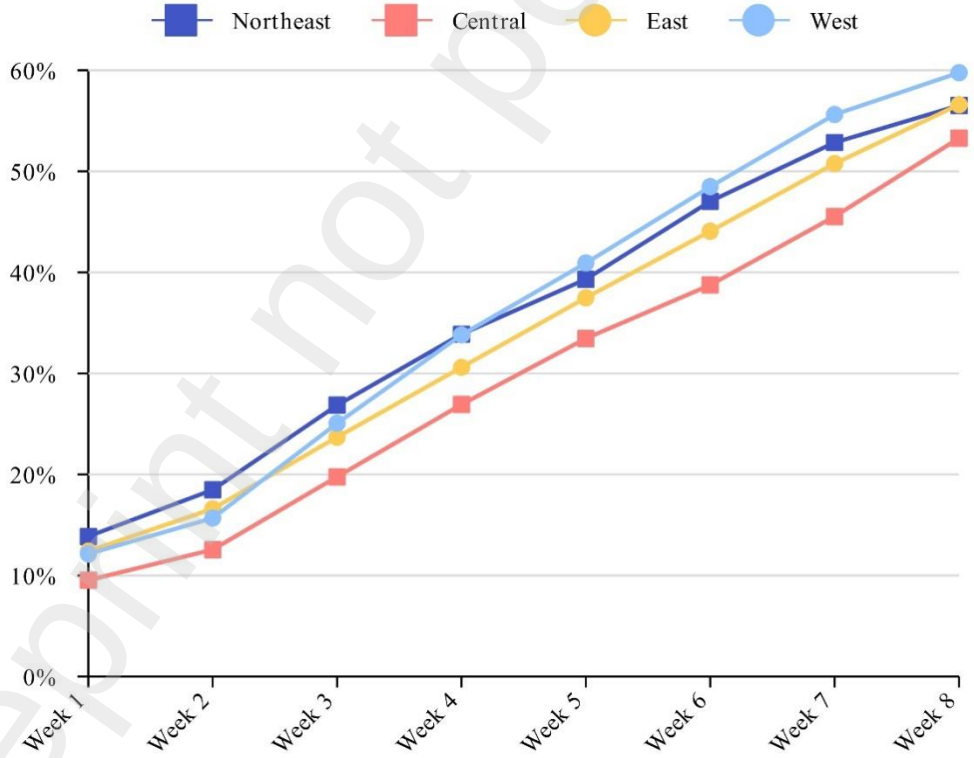

Figure 3. Variations in the TRI across Regional Cities in China During the Q1 of 2020.

By the end of the Q1, the TRI varied among areas, as illustrated in Figure 3. The western area led the fray with the index touching 59.76%, the highest among all regions. The northeastern and eastern areas closely followed, displaying indices of 56.52% and 56.60% respectively. In the central region, relatively

more impacted by the pandemic, the index landed at 53.28%, slightly lower than other parts. These figures delineate the epidemic control scenario and the recuperation extent of urban transportation vitality in different areas, tangentially endorsing the transportation activity levels [16].

As for the implications of forecasting the TRI, firstly, it serves as an effective early warning mechanism, signalizing potential transportation issues to policy-makers and planners, subsequently prompting timely adjustments. Secondly, through the forecasting of this index, policy-formers can anticipate the economic development of cities with enhanced precision, granting data support for policy formulation. Ultimately, this is substantially enlightening for understanding post-disaster urban revitalization, evaluating transport recovery, and policy-making processes.

1.3 Contributions

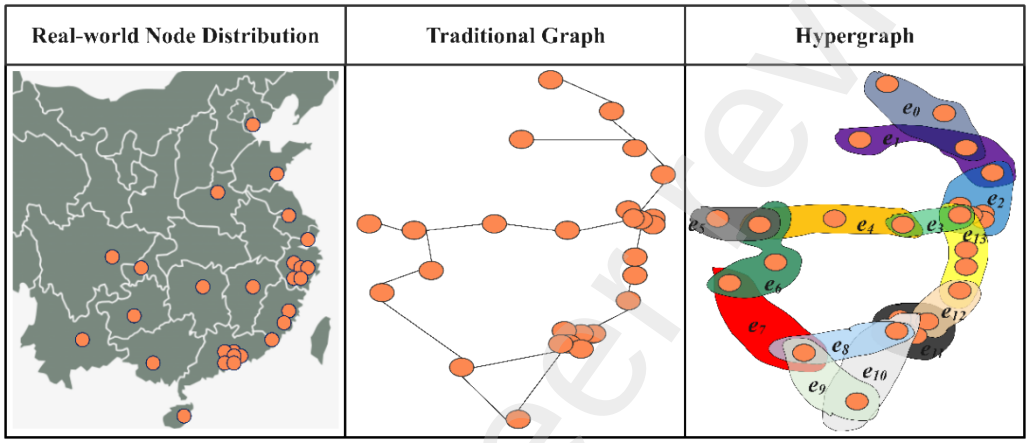

Figure 4. A comparative delineation between traditional graph and hypergraph for the depiction of spatial relationships among cities.

Graph neural networks have been extensively deployed in the investigation of TRI forecasting [17], where cities are regarded as nodes and the distances between cities as edges, thus effectively illuminating the spatial correlation traits among cities. Yet, the traditional graph models bear certain limitations when addressing complex instances [18]. For illustration, these models typically presuppose only pairwise interactions between nodes, ignoring the actual scenario where high-dimensional influences on the TRI might emanate from the interplay among multiple cities (three or more). Such multidimensional interactions are not ideally handled in traditional graph models. Likewise, these models consider each edge to represent a solitary relationship between two cities, potentially overlooking the global or high-dimensional influence mechanisms, and as a result, underestimating the complexity of the interaction effects. As for hidden non-linear structures or complex compound effects, traditional graph models fall short in their treatment capabilities. However, the advent of hypergraph models elegantly addresses such issues [19]. As demonstrated in Figure 4, hypergraph models inherently support and manage more complicated, higher-dimensional interactions. The *e* denotes the edge interlinking multiple urban centers in the hypergraph schema. Whether the framework is a three-dimensional interaction among various cities or high-dimensional interaction among even more urban environments, the model processes this with efficacy. In addition, hypergraph models model in a more intricate manner, accommodating higher-order and more complex structures, thereby facilitating a deeper understanding of global or high-dimensional influence mechanisms and circumventing the underestimation of complex interaction effects. In handling non-linearity, the hypergraph model likewise excels, effectively capturing hidden non-linear structures or complex compound effects [20]. Therefore, compared to graph neural network models, hypergraph models evince greater potential and strength in revealing high-dimensional interactions, handling global or high-dimensional influence mechanisms, and capturing hidden non-linear structures

or complex compound effects. They confer an advantage in delineating high-dimensional and non-linear, introducing new possibilities for TRI forecasting.

This study not only surmounts the limitations incumbent in traditional graph models related to handling high-dimensional interactions, global or high-dimensional impact mechanisms, and non-linear structures but also pioneers a fresh approach to forecasting TRI using a spatio-temporal hypergraph model. The principal contributions of this study can be succinctly distilled into three domains:

1. Contrasting the traditional graph models that deal merely with individual interactions between pairs of nodes and low-dimensional relationships, this study integrates hypergraph models to capture and delineate high-dimensional and nonlinear interactions across multiple metropolises, thereby markedly enhancing the model's capacity to represent complex relationships between nodes.

2. This study conceptualizes a novel hypergraph convolution module that capably learns the spatial correlation characteristics of city nodes. Additionally, it proposes a temporal convolution module to learn the intricate time-dependency features of TRI data, thereby equipping the model to better comprehend and forecast TRI.

3. Experiment results on a real-world dataset demonstrate a composite 51.66% reduction in predictive error when juxtaposed with the established benchmarks of this study, thereby attesting to the efficaciousness of the hypergraph model coupled with hypergraph convolution and temporal convolution modules in the endeavor to forecast the TRI.

2 Literature Review

The guiding principle of TRI research is indubitably time-series forecasting. Eminent in the realms of statistical methodologies, Autoregressive Integrated Moving Average (ARIMA) [21] emerges as a comprehensive tool employed on a routine basis for time-series forecasting. Considering the autocorrelation intrinsic to data, the ARIMA model tends to stabilize time series data prior to modeling through differentiating procedures. Transitioning to the field of Machine Learning, the Support Vector Machine (SVM) [22] constitutes a supervised learning algorithm chiefly utilized in classification and regression objectives. In the context of time-series forecasting, SVM takes time-series data as input attributes, and designates the forthcoming time-step as the output objective [23]; thus, striving to identify the optimal hyperplane that distinguishes data points in a high-dimensional space best. TRI time-series forecasting involves forecasting variations in data within a realm characterized by its intricacies, spatially and nonlinearly - a realm, where data invariably exhibits complex interdependencies and nonlinear connections. Being a linear model, ARIMA may find itself grappling with the intricate and nonlinear nature of TRI data. While SVM is capable of capturing nonlinear relations, it confronts challenges in effectively modeling the spatial dependencies and complex patterns inherent to TRI time-series data [24]. Given the intricacies of spatial relationships and nonlinear features in TRI time-series data, traditional models such as ARIMA and SVM fall short of providing accurate and robust predictions. The Graph Convolutional Network (GCN) [25], a specialized deep learning model, is proficient in learning node attributes and relationships effectively. In predictive tasks relating to interurban TRI time-series data, cities and their reciprocal connections can be represented as a graph, wherein each city is a node and the connectivity between cities constitutes the edges. On one hand, GCN adeptly utilizes the topology of interurban structures [26]. By harnessing such nodal and edgy insights, GCN captures the complex spatial dependencies between cities. The spatially proximate cities potentially influence the traffic flow of the target city. On the other hand, the integration of GCN with current temporal models allows for capturing spatio-temporal dynamic variation in time-series data [27]. This capacity to simultaneously model spatial and chronological information grants GCN a distinction in dealing with convoluted prediction tasks. For instance, to address the inability of existing GCN methods to accurately sketch the interaction between fine and coarse grain information in multi-granularity spatial-temporal patterns, Zhang et al. designed a

self-adaptive multi-level spatio-temporal model that learns from distinct-level coarse grain graphs [28]. Similarly, Du et al. propounded a multi-scale feature-enhanced spatio-temporal model based on attention mechanism and GCN that dynamically augments dependencies of spatio-temporal features [29].

The TRI has emerged as a pivotal indicator for assessing urban traffic resurgence post the COVID-19 pandemic. Prior research endeavors have deployed sophisticated spatio-temporal models, amalgamating TRI data, pandemic statistics, and urban spatial relationships to actualize TRI forecasting. Lv et al. have pioneered a spatio-temporal model leveraging the GCN to capture the spatial correlation features of city geographies and harmoniously integrate varying scales of COVID-19 data into TRI datasets, culminating in pandemic information amalgamation and TRI forecasting [30]. Furthermore, a model christened DeepMeta-TRI, conceived by Wang et al., is meticulously tailored for TRI forecasting. It orchestrates a deep spatio-temporal meta-learning structure which deftly integrates external auxiliary information [31]. The DeepMeta-TRI framework encompasses a meta-GCN module and a meta-temporal convolution module capable of assimilating and handling diverse external datasets. In the quest to enrich spatial topological relationships amidst cities, DeepTree-TRI elegantly reinvigorates city interconnectivity by introducing a tree-based architecture, thereby capturing hierarchical and local pathway spatial correlations among urban nodes [32]. In a bid to tackle the intrinsic spatio-temporal pivotal traits of intercity dynamics within the holistic topological network, the DeepST-AM engineers a spatio-temporal model imbued with a spatio-temporal attention mechanism to wield TRI forecasting [33]. The DeepST-AM also contemplates the variegating temporal cycles' influence on TRI transmutation within the current epoch hence reinforcing the model's spatio-temporal prowess. Nevertheless, all aforementioned models are predicated on conventional graph representations, sans the integration of hypergraph into TRI forecasting.

Hypergraph, heralded for its more intricate capacity to delineate higher-dimensional relationships, present an untapped potential for enhancing the comprehension and construction of convoluted topological networks. Within TRI forecasting, the hypergraph can accentuate the representational competency of complex spatial networks by synergizing with temporal convolution models to apprehend finer-grained spatio-temporal correlation attributes, thus fostering heightened prediction accuracy unattainable by traditional graph models.

3 Preliminaries

3.1 Problem Definition

The TRI forecasting serves as a time-series forecasting endeavor [34], where each node in the graph signifies data calculated based on specific temporal intervals. At the time step t, this study employes x_i^t to denote the TRI value of node i. Consequently, $X^t = \{x_1^t, x_2^t, ..., x_N^t\} \in \mathbb{R}^N$ epitomizes the TRI values of all nodes at time step t. Furthermore, $X = \{X^1, X^2, ..., X^T\} \in \mathbb{R}^{N \times T}$ encapsulates the TRI values of all nodes over T time instances. To forecast, this study designates y_i^t as the TRI value of node i at a future moment t. Similarly, $Y^t \in \mathbb{R}^N$ delineates the TRI values of all nodes at a future instant t, while $Y = \{y^1, y^2, ..., y^{T_p}\} \in \mathbb{R}^{N \times T_p}$ corresponds to the TRI values of all nodes within a future time T_p span. For each node i, this study monitors its COVID-19 pandemic data, denoted by $m_i^t \in \mathbb{R}^c$ at time step t, where c represents the data categories like confirmed cases, recovered cases, deceased cases, and suspected cases. Therefore, $M^t = \{m_1^t, m_2^t, ..., m_N^t\} \in \mathbb{R}^{N \times c}$ symbolizes the pandemic data of all nodes at time step t, and $M = \{M^1, M^2, ..., M^T\} \in \mathbb{R}^{N \times T \times c}$ encapsulates the pandemic data of all nodes across different instances. Given the historical TRI and COVID-19 pandemic data of all nodes over the past time interval T, represented by X and M respectively, our objective lies in predicting the TRI data of

future time duration T_p denoted by Y. This entire process can be encapsulated as $Y = f(X,M,H)$, where H signifies the hypergraph representation of urban nodes. Here, f denotes a function from $\mathbb{R}^T$ to $\mathbb{R}^{T_p}$, modeling the predictive task by facilitating feature mapping from historical data to future predictive data.

3.2 Hypergraph Representation

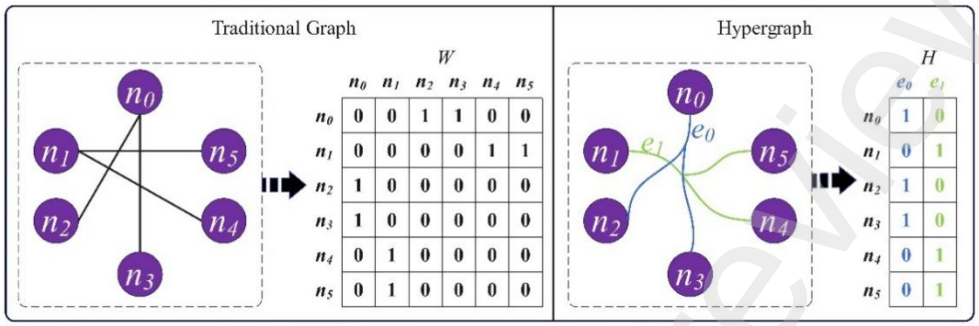

Figure 5. Representations of traditional graph and hypergraph.

Diverging from the traditional graph structures, the hypergraph feature a hyperedge that connect two or more vertices, as illustrated in Figure 5. A hypergraph is characterized as $G = (V,E,\Delta)$, encompassing a set of vertices V and a collection of hyperedges E. Each hyperedge is endowed with a weight via W, akin to the weight diagonal matrix in conventional graph [35]. The hypergraph G can be delineated by an association matrix H of dimensions $|V| \times |E|$. Moreover, D_e and D_v stand respectively for the diagonal matrices of edge degrees and vertex degrees. The $\Omega(f)$ constitutes a regularization term for the hypergraph (in this instance, the Laplacian representation of the hypergraph) as denoted in Equation (1), where f signifies a regression function and T denotes the transposition operation, $\Delta = I - \Theta$, and $\Theta = D_v^{-\frac{1}{2}} H W D_e^{-1} H^T D_v^{-\frac{1}{2}}$.

$$\Omega(f) = f^T \Delta \tag{1}$$

4 Methodology

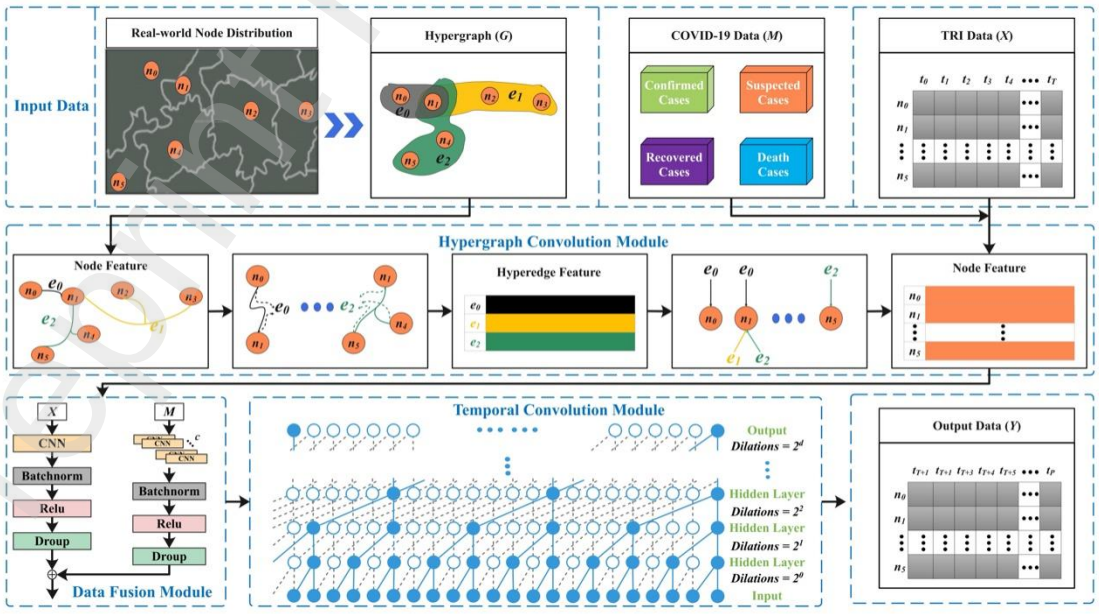

Figure 6. The architectural design of STHCN.

An innovative architecture denoted as STHCM is unveiled in this study, wherein Figure 6 delineates its architectural design. This architecture ingests three types of data: hypergraph G outlining spatial relations of urban nodes, COVID-19 data M encompassing four types of information (confirmed cases, recovered cases, deceased cases, and suspected cases), and the historical data X of TRI. Upon the commencement of the workflow within the STHCM architecture, the hypergraph is transmuted via the hypergraph convolution module, mapping the features of the urban nodes to hyperedge features. Given that the historical data of TRI is organized based on node characteristics, this module eventually maps the hyperedge features back to node features [36], facilitating an amalgamation with the TRI data features in consequential steps. Subsequently, the data fusion module employs residual connections to integrate data from COVID-19 sources. This methodology adeptly minimizes information attrition and augments model learning capacity. Ultimately, the TRI data, having fused node spatial features and COVID-19 data features, is fed into the temporal convolution module formed of dilated and causal convolutions. This module is capable of apprehending dependency features of TRI data as they evolve over time. Post normalization of data, there emerges the final output of the model, predicting the future TRI values for each urban node.

4.1 Hypergraph Convolution Module

Consider a hypergraph $G = (V,E,\Delta)$ endowed with N nodes. Linked to this hypergraph is the semi-definite Laplacian matrix Δ. Employing eigen decomposition of the form $\Delta = \Phi\Lambda\Phi^T$, one can isolate orthogonally invariant eigenvectors $\Phi = diag(\emptyset_1,...,\emptyset_N)$ alongside a diagonal matrix $\Lambda = diag(\lambda_1,..., \lambda_N)$ hosting non-negative eigenvalues. Within the schema of the hypergraph, the Fourier transform of signal $X = (x_1,...,x_N)$ is defined as $\hat{X} = \Phi^T X$. Herein, the eigenvectors are considered the Fourier basis and eigenvalues interpreted as frequencies. The spectral convolution between the signal X and a filter g can be denoted as Equation (2).

$$\mathrm{g} * X = \Phi((\Phi^T g)\odot(\Phi^T X)) = \Phi g(\Lambda)\Phi^T X \tag{2}$$

In the equation, the symbol $\odot$ denotes the Hadamard product while $g(\Lambda) = diag(g(\lambda_1),...,g(\lambda_N))$ represents the function of Fourier coefficients. However, the forward and reverse Fourier transformations demand computational complexity of the order $O(n^2)$. One can refer to the work to counter this challenge, parameterizing $g(\Lambda)$ with a *K*-order polynomial [37]. This study employs a truncated Chebyshev expansion as this polynomial. The Chebyshev polynomial $T_k(\mathrm{x})$ can be recursively computed through $T_k(\mathrm{x}) = 2xT_{k-1}(\mathrm{x}) - T_{k-2}(\mathrm{x})$, satisfying $T_0(\mathrm{x}) = 1$ and $T_1(\mathrm{x}) = \mathrm{x}$. Thus, $g(\Lambda)$ can be parametrized as Equation (3).

$$g * X \approx \sum_{k=0}^{K} \theta_k T_k(\tilde{\Delta})x \tag{3}$$

The $T_k(\tilde{\Delta})$ is the *K*-order Chebyshev polynomial based on a scaled Laplacian matrix, defined as $\tilde{\Delta} = \frac{2}{\lambda_{\max}}\Delta - I$. Notably, the Equation (3) omits the calculation of the Laplacian matrix's eigenvectors, including only the matrix's power, addition, and multiplication, thus attenuating computational complexity. Given the hypergraph Laplacian matrix is already adept in capturing high-order node correlation, this method can further restrict the convolution operation order to *K*=1, a suggestion based on the scale adaptability to satisfy $\lambda_{\max} \approx 2$. Consequently, the convolution operation can be further simplified as Equation (4).

$$g * X \approx \theta_0 \mathrm{x} - \theta_1 D^{-\frac{1}{2}} H W D_e^{-1} H^T D_e^{-\frac{1}{2}} x \tag{4}$$

The θ_0 and θ_1 are the parameters of filters across all nodes. This study adopts single variable θ to avoid overfitting, as can be defined by Equation (5). Thus, the convolution operation simpifies further to

Equation (6).

$$\begin{cases} \theta_0 = -\frac{1}{2}\theta \\ \theta_0 = \frac{1}{2}\theta D_{\mathrm{v}}^{-\frac{1}{2}} H D_e^{-1} H^T D_v^{-\frac{1}{2}} \end{cases} \tag{5}$$

$$g * X \approx \frac{1}{2}\theta D_{\mathrm{v}}^{-\frac{1}{2}} H(W+I) D_e^{-1} H^T D_v^{-\frac{1}{2}} x \approx \theta D_{\mathrm{v}}^{-\frac{1}{2}} H \mathrm{W} D_e^{-1} H^T D_v^{-\frac{1}{2}} \mathrm{x} \tag{6}$$

Additionally, the $(W+I)$ can be viewed as the weight of the edges, with W initialized as the unit matrix, implying all hyperedges possess equal weight. Given a hypergraph signal $X \in R^{n \times C_1}$ with N nodes and C_1 dimensional features, the hyperedge convolution can be expressed as Equation (7). Here, $\mathrm{W} = diag(\mathrm{w}_1,\ldots,w_N)$, and $\Theta \in R^{C_1 \times C_2}$ represents parameters to be learned during the training process. The filter Θ acts on nodes of the hypergraph to extract the relevant features. Following convolution, we achieve $Y \in \mathbb{R}^{C_2}$.

$$Y = D_{\mathrm{v}}^{-\frac{1}{2}} H \mathrm{W} D_e^{-1} H^T D_v^{-\frac{1}{2}} X \Theta \tag{7}$$

Regarding the hypergraph convolution module, this study explores high-order correlation features of data. As illustrated in Figure 6, the hypergraph convolution module facilitates transformation of node-edge-node features, thus better utilizing the hypergraph structure for feature extraction. More specifically, the initial node features are processed by a learnable filter matrix. They shape hyperedge features, aggregating node features based on the edges, accomplished by multiplication with $H^T \in \mathbb{R}^{\mathrm{E} \times N}$. Eventually, output node features are obtained by aggregating relevant hyperedge features. D_v and D_e in Equation (7) deliver normalization impacts. Therefore, the hypergraph convolution module is proficient in efficient extraction of high-order correlations of the hypergraph through node-edge-node transitions.

4.2 Data Fusion Module

In an endeavor to tease out the innate correlation between TRI data and COVID-19 epidemic statistics, a data fusion module is devised with the explicit intent of amalgamating COVID-19 epidemic data with TRI data. Descriptive parameters encapsulated within the COVID-19 epidemic data encompass confirmed, recovered, deceased and suspected cases per city, among others. The structure of the data fusion module, illustrated in Figure 6, is orchestrated to accomplish this aim. Input data integrate TRI data X and COVID-19 epidemic data M. Convolutional operations serve as the workhorses for extracting the rudimentary features of these two types of data. Within the epidemic data M, data corresponding to various types symbolize different channels. Information obtained from these distinct channels undergoes convolutional learning which may be construed as a measure to identify and adjust the importance levels of these datasets. Following the acquisition of primitive features, the data are subjugated to BatchNormalization and Dropout treatments. BatchNormalization operation imparts stability to the data distribution whereas the Dropout operation counteracts model overfitting [39]. Subsequently, the Rectified Linear Unit (ReLU) function [40] is deployed as an activation regimen to augment the model's non-linear fitting capacity. Upon the completion of these operations, data fusion is achieved through a weighted method.

4.3 Temporal Convolution Module

During the process of TRI time-series forecasting, a residual block composed of a branch is employed in this study. This branch leads to a series of transformations denoted as F, where its output is amalgamated with the input x as illustrated in Equation (8).

$$\mathrm{y} = Activation(x + F(x)) \tag{8}$$

This structure is conducive for network layers to learn and execute fine-tuning on identity mapping rather than comprehensively shifting [42], a method that has demonstrated its efficacy particularly in architecting profoundly deep networks. The receptive field of the temporal convolution module is conjointly determined by the network depth, the size of the filter, and the dilation factor. When designing

essentially critical, larger, and deeper temporal models for conducting TRI forecasts, the stability of the model comes to play a pivotal role. For instance, a deeper network is required for forecasts that may depend on long-term historical TRI data. Specifically, each layer harbors numerous filters for extracting features.

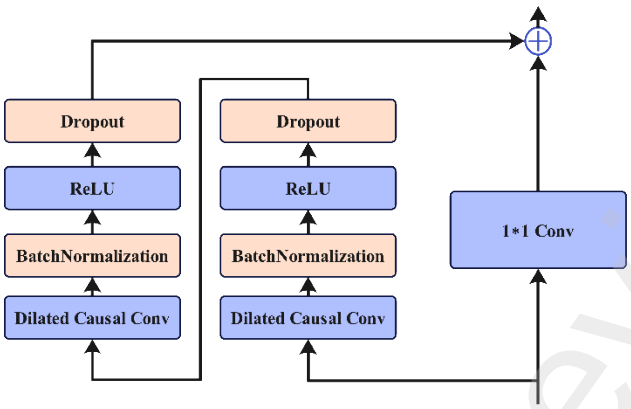

Figure 7. The residual network of the temporal convolution module.

During the assembly of the temporal convolution module for TRI forecasting, a standard residual module is utilized to replace the convolution layer, as portrayed in Figure 7. Each residual block is assembled from two layers of dilated causal convolution and non-linear behavior, where this module employes a ReLU function. Normalization is conducted on the convolution filters using weight normalization Batchnorm in the normalization process. Moreover, a Dropout is added after each dilated convolution to achieve regularization. Nevertheless, the input is directly added to the output from the residual function, and the input and output possess different shapes. To rectify the discrepancy in input-output shapes, this module utilized an auxiliary 1×1 convolution to ensure that the operation of element-wise addition $\oplus$ can process tensors of the same shape.

A key theoretical aspect of the TRI forecasting method stipulates that information from the future should not reverse into preceding information for model training. Hence, this module adopts causal convolution where the output at time point t only convolutes with elements from a layer earlier than t time point. A principal challenge of this fundamental design is reaching a long-term effective record, necessitating the construction of a profoundly deep network or the extensive filters. The causal convolution can only look at the historical depth of the network, which complicates the application of causal convolution on time-series tasks, particularly instances requiring long historical data. Our resolution strategy herein is to resort to dilated convolutions, thereby enlarging the receptive field, demonstrating exponential features. To elaborate, for a one-dimensional sequence input x and filter $\Theta:\{0,\ldots,k-1\}\rightarrow\mathbb{R}$, the dilated convolution operation F for elements s in the sequence is defined as depicted in Equation (9).

$$F(s) = \sum_{i=0}^{k-1} f(i) \cdot x_{s-d \cdot i} \tag{9}$$

Wherein, the d stands for the dilating factor, the k denotes the filter size, and $(s - d \cdot i)$ serves to reflect the direction of the past. Introducing a fixed stride between every two adjacent filters is equivalent to dilating. When $d = 1$, the dilated convolution simplifies to standard convolution. Employing a larger dilation facilitates the top layer output to represent a broader range of input, thereby effectively expanding the receptive field of the convolution network. This provides two methods to augment the receptive field of TRI forecasting: selection of a larger filter size k, and increasing the dilation factor d. The effective history of a certain layer is $(k-1) \times d$. Analogous to using dilated convolution, this module let network depth and dilation factor grow exponentially. This ensures that each input in the effective history is "touched" by some filters, while also allowing for the use of deep networks to realize a grand effective history.

5 Experiments

5.1 Dataset Elucidation

This study leans heavily on two principal data sources: the TRI data and the COVID-19 pandemic data. The TRI data stem from the Gaia Data Plan [42], processed intricately from a wealth of trajectory data and transport performance indices from the Didi Doche platform. Through meticulous methods such as fitting, cross-validation, and weighting procedures, meaningful insights are gleaned from the raw data, culminating in the final TRI dataset. This dataset spans continuously from February 10, 2020, to June 30, 2020, covering 27 major cities within China. The COVID-19 pandemic data, furnished by the National Health Commission of China [43], encompass four categories of COVID-19 data for these 27 cities: confirmed count, suspected count, cured count, and death count. Prior to deploying these datasets, an exhaustive and exacting data cleaning and curation process took place. This included the removal of data noise, imputation of missing data, and more to uphold the veracity and reliability of the experiment.

5.2 Experimental Design

Within the cadre of this experimental procedure, the batch size is stipulated at 16, coupled with a learning rate of 0.01 that undergoes a tenfold decrement for every 50 epochs. The overall count of these training epochs is established at 150. The selected optimizer for this process is the *StepLR* [44], while the chosen loss function is L_2. A detailed portrayal of the training process is exemplified in Algorithm 1.

The hypergraph convolution module employs a single layer of hypergraph convolution, where the number of nodes aligns with the city nodes defined within the dataset. Node characteristics incorporate the TRI data from the preceding 12 days of all cities, which is utilized to anticipate the data for the ensuing 1, 3, and 7 days. The convolutional kernel size for both the data fusion module and time convolution module is designated as 3×3. Within these, the dilation rate of the convolution adjusts in accordance with the power of 2. This temporal convolution module is constituted by seven layers of residual connections.

Algorithm 1. Model Training and Testing Process.

IINPUT

$\theta = \{(x_n, y_n)\}_{n=1}^{N}$, a TRI dataset for training.

$\theta' = \{(x_{n'}, y_{n'})\}_{n'=1}^{N'}$, a TRI dataset for testing.

A, an adjacency matrix of nodes.

α, the learning rate, whose initial value is 0.01.

λ, the step size, whose initial value is 5.

gamma, the decay rate, whose initial value is 0.7.

y', spatial-temporal model.

TRAIN

1 Calculate the hypergraph correlation matrix H from the A.
2 Repeat
3 for $n = 1, \ldots, N$ do
4 Select samples $\{(x_n, y_n)\}$ from the training set θ.
5 $y' = model(x_n, \mathrm{H})$, feedforward calculates the features of each model layer until the last layer.
6 Calculate loss, $L_2 = \frac{1}{n}\sum_{i=1}^{n} (y - y')^2$
7 Backpropagation updates model gradients, $StepLR(RMSprop, \alpha, \lambda, gamma)$.
8 End

TEST

9 Repeat
10 for $n' = 1, \ldots, N'$ do
11 Select samples $\{(x_{n'}, y_{n'})\}$ from the testing set θ'.
12 $y = y'(x_{n'}, \mathrm{H})$, feedforward calculates the features of each model layer until the last layer.

13 Calculate loss and evaluate performance metrics on the test set.
14 End
OUTPUT
y, the prediction result of the model.

In this manuscript, three regressive indices are established to evaluate the forecast results of the model, as demonstrated in Equations (10) to (12). The Mean Absolute Error (MAE) [45] characterizes the average absolute discrepancy between predicted and true values, providing a uniform weight to every error. It is easily perceivable and displays a robustness against outliers, with the magnitude of its value serving as a direct marker of the predictive model's precision. The Root Mean Square Error (RMSE) [46]holds considerable emphasis on more substantial errors. Thus, if the model's predictions are largely precise for the majority of samples, but a few demonstrate significant deviation, the RMSE will scale up. Utilizing RMSE as a criterion elicits a more comprehensive reflection of the model's predictive stability. The Mean Absolute Percentage Error (MAPE) [47] puts forth a percentage error, significantly beneficial in comparing predictive errors across disparate data scales. Consequently, a smaller value symbolizes more accurate predictions.

$$\mathrm{MAE} = \frac{1}{n}\sum_{i=1}^{n}\left|y_i - \hat{y_i}\right| \tag{10}$$

$$\mathrm{RMSE} = \sqrt{\frac{1}{n}\sum_{i=1}^{n}\left(y_i - \hat{y_i}\right)^2} \tag{11}$$

$$\mathrm{MAPE} = \frac{1}{n}\sum_{i=1}^{n}\left|\frac{y_i - \hat{y_i}}{y_i}\right| \times 100\% \tag{12}$$

This experiment prioritizes six baseline models: ARIMA, SVM, GCN, DeepMeta-TRI, DeepTree-TRI, and DeepST-AM. Regarding time-series problems, ARIMA, due to its lucid statistical connotations and typical application scenarios, is regarded as a fundamental and significant comparison method. SVM, a supervised learning method, demonstrates commendable performance across various quandaries, given appropriate parameter configuration. This experiment takes into account the model's ability to process graph-structured data, where GCN, with its distinctive adjacency matrix and Laplacian matrix processing methods, excels in capturing graph structure information. Lastly, this study considers the model's scalability and performance upon specific tasks, where DeepMeta-TRI, DeepTree-TRI, and DeepST-AM are tailor-made for specific TRI prediction tasks, assimilating spatio-temporal relationships using different strategies and providing robust modeling capacity for the target task. Collectively, these benchmarks span a spectrum of foundational to cutting-edge techniques, allowing for a comprehensive and in-depth comparative analysis that can underpin our research. Detailed configuration information of these benchmarks are as follows:

1. ARIMA: Widely employed for time-series forecasting, ARIMA's order of autoregressive parts and differences are configured at one, with the moving average orders designated at 0.5.

2. SVM: A supervised learning model, SVM is primarily utilized for classification and regression analysis. Its hard margin constant is set to 1, kernel type configured as *rbf*, with a gamma set at 0.5.

3. GCN: Establishes adjacency and Laplacian matrices in the spectral domain, using the Chebyshev polynomial method to approximate the Fourier transform process.

4. DeepMeta-TRI: DeepMeta-TRI treats additional information as metadata, capturing the rich and complex dynamic spatio-temporal relationships during the COVID-19 period and consequently accomplishing the TRI prediction task.

5. DeepTree-TRI: Leveraging tree structures, DeepTree-TRI mines spatial characteristics between cities, paired with a temporal convolution module, it extracts spatio-temporally relevant traits from TRI data.

6. DeepST-AM: DeepST-AM adopts a spatio-temporal attention mechanism to highlight the significance of spatial relationships between different cities, and through Gauss temporal convolution

strategies, it achieves the learning of TRI temporal features.

5.3 Comparison and Analysis of Experimental Results

5.3.1 Statistical Analysis of Results

Each model showcases distinct characteristics in terms of forecasting error as well as stability, as illustrated from Figure 8 to Figure 10. Notably, ARIMA, a commonly employed time-series prediction model, surface as the least effective across all models, indicating its rather lower prediction precision. SVM, a model based on supervised learning, even though surpasses ARIMA in predictive outcomes, its precision leaves room for enhancement when it comes to medium to long-term predictions. GCN, capitalizing on the attributes of graph networks, gives rise to superior predictive outcomes compared to SVM and ARIMA, thus promising unparalleled prediction accuracy and stability. Regarding the RMSE, DeepMeta-TRI, DeepTree-TRI, DeepST-AM, and STHFM noticeably outstrip the former three models with their RMSE all falling below 3.5, evincing their sound prediction stability. DeepMeta-TRI further refines the predictive performance, excelling especially in capturing intricate dynamic spatio-temporal relations amidst the COVID-19 epoch. For instance, its performance on MAE distinctly outstrips the former three models, only marginally rising from 2.59 to 2.79, indicating the high predictive precision and stability maintained by this model. DeepTree-TRI exploits the tree structure and temporal convolutional units, considerably enhancing the predictive accuracy and stability. Whereas DeepST-AM underscores its commitment to prediction accuracy by employing the spatio-temporal attention mechanism. Despite the augmenting error owing to increased time scale, it continues to maintain an overall low error level. Conclusively, STHFM emerges as the most laudable among all the models, consistently delivering superior performance across different assessment indicators and time scales, thereby solidifying its exceptional predictive precision and stability. Drawn against ARIMA, SVM, GCN, DeepMeta-TRI, and DeepTree-TRI models, STHFM distinctly minimizes errors. The average error reduction percentages with respect to SHTFM for each model stand at 74.39%, 68.09%, 64.97%, 34.47%, and 16.38%, cumulating to an average error reduction rate of 51.66%. Taking an overview, one can discern an incremental improvement in the predictive effect from ARIMA to STHFM among all models, illuminating the notable advantage held by the models that merge deep learning and spatio-temporal theories in tackling complex spatio-temporal forecast tasks.

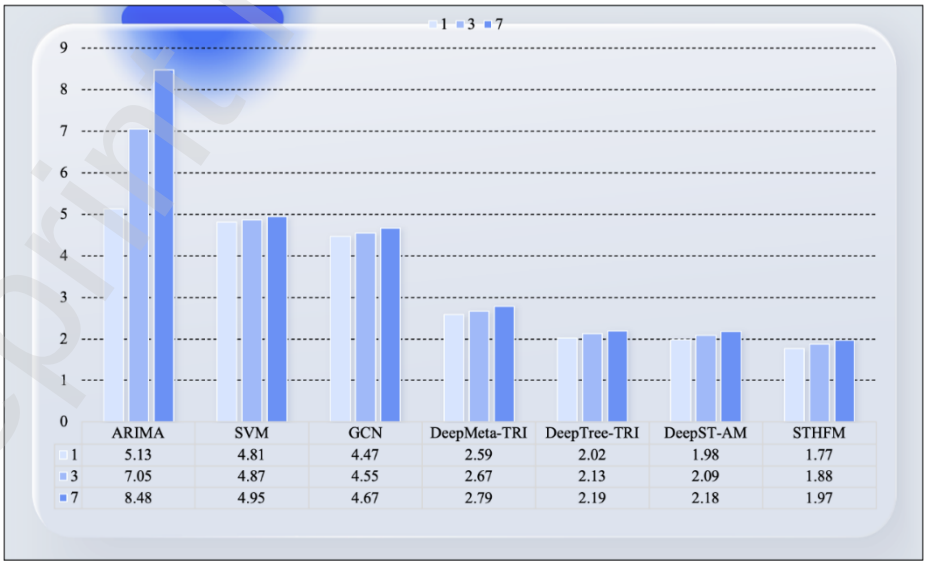

	ARIMA	SVM	GCN	DeepMeta-TRI	DeepTree-TRI	DeepST-AM	STHFM
1	5.13	4.81	4.47	2.59	2.02	1.98	1.77
3	7.05	4.87	4.55	2.67	2.13	2.09	1.88
7	8.48	4.95	4.67	2.79	2.19	2.18	1.97

Figure 8. Statistical results regarding the MAE.

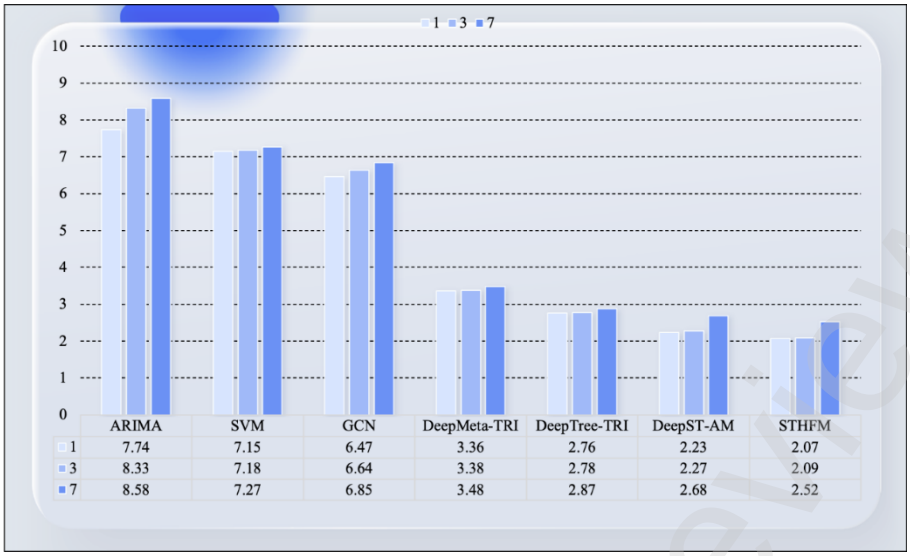

	ARIMA	SVM	GCN	DeepMeta-TRI	DeepTree-TRI	DeepST-AM	STHFM
1	7.74	7.15	6.47	3.36	2.76	2.23	2.07
3	8.33	7.18	6.64	3.38	2.78	2.27	2.09
7	8.58	7.27	6.85	3.48	2.87	2.68	2.52

Figure 9. Statistical results regarding the RMSE.

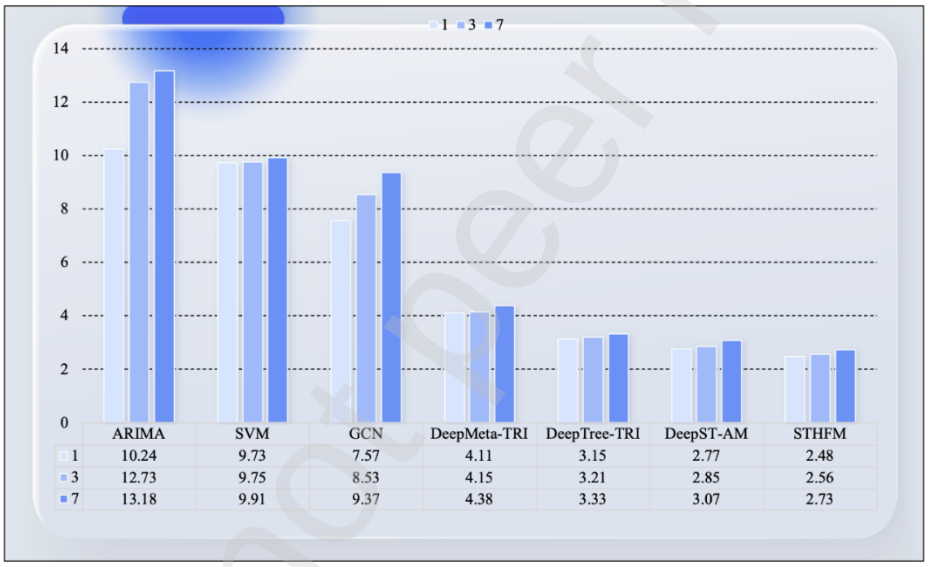

	ARIMA	SVM	GCN	DeepMeta-TRI	DeepTree-TRI	DeepST-AM	STHFM
1	10.24	9.73	7.57	4.11	3.15	2.77	2.48
3	12.73	9.75	8.53	4.15	3.21	2.85	2.56
7	13.18	9.91	9.37	4.38	3.33	3.07	2.73

Figure 10. Statistical results regarding the MAPE.

5.3.2 Discussions

In above panorama of predictive modeling, various models exhibit different performance characteristics. In most cases, models adhere closely to actual values, but DeepMeta-TRI and DeepST-AM models tend to perform suboptimally when predicting smaller TRI values. Nevertheless, over time, prodicted values from these models tend to gradually coalesce with true values, as illustrated in Figure 11. In stark contrast, predictions made by the GCN model consistently fall short of true values in all scenarios.

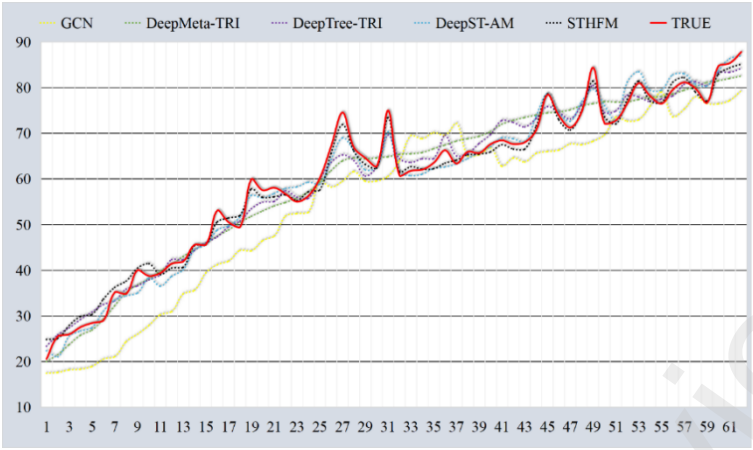

Figure 11. Temporal comparison of model predicted values and true values.

The deployment of residual analysis in assessing the correlation between the predicted and true TRI values exposes a pronounced advantage [48]. Primarily, residual plots—that encapsulate the discrepancy between real-world values and model predicted values—demystify the pattern of prediction errors [49], providing a cogent representation of the prediction accuracy and bias. Notably, if the dispersion of a specific scattered group diverges noticeably from others, it implies that the model performance may vary across different data thresholds. Furthermore, the residual analysis aids in pinpointing anomalies and scrutinizing the congruence between predicted values and true values. The comparative results of the residual analysis for this experimental model are demonstrated in Figure 12. ARIMA, a quintessential model for time series forecasting, predominantly focuses on the traits of these series, overlooking potential spatial correlations and nonlinear trends [50]. Accordingly, its performance falls relatively short in the task of complex TRI forecasting. The SVM models help to bridge this gap by boasting the capacity to process non-linear problems, but struggle with exploiting spatial correlations [51], thereby potentially underusing hidden information under certain conditions. Conversely, GCN models, strengthened by graph structures, are adept at handling spatial correlations but could require additional support for time correlation processing [52]. Unlike the models mentioned above, DeepMeta-TRI, DeepTree-TRI, DeepST-AM, and STHFM incorporate mechanisms to manage both temporal and spatial characteristics. They employ deep learning techniques to capture the complexities and non-linearity inherent in the data. Specifically, DeepMeta-TRI flexibly accommodates additional data, capturing rich spatio-temporal dynamic correlations during the COVID-19 period. DeepTree-TRI brings in a dendritic structure to mine city-to-city spatial traits, thereby facilitating a more robust learning of spatial characteristics. DeepST-AM, accentuating a spatio-temporal attention mechanism, gets better at understanding inherent data characteristics, also enhancing prediction accuracy. Shouldering the complex TRI prediction challenge, the STHFM unveils primary advantages like enhanced nodal fusion capabilities, effective management of long-term temporal dependencies, and proficient time series analysis [53]. Its hypergraph structure enables hyperedges to connect more nodes [54], effectively representing manifold relations and considering a more comprehensive and rich set of information. Moreover, compared to other models, STHFM better capitalizes on long-term temporal dependent characteristics of TRI data. Through residual connections, it mines and learns the features and trends of data under long-term time windows [55], leading to more precise predictions. Lastly, the STHFM integrates a temporal convolution module fundamental to dilated and causal convolutions, uncovering hidden information and patterns within the time series, thereby bolstering forecasting effect. These attributes equip STHFM with superior performance in TRI prediction tasks.

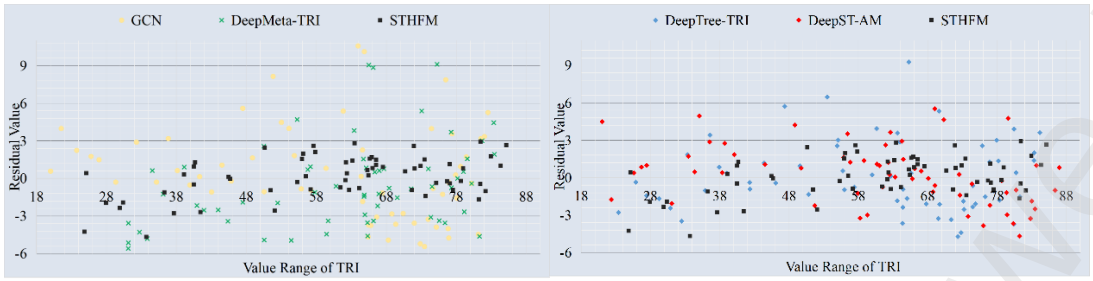

Figure 12. Comparative analysis of residuals between model predicted values and true values.

5.3.3 Ablation Experiment

Within the context of the STHFM, the HCM, TCM, and the DFM all play pivotal roles, as illustrated in Figure 13. The core function of the HCM rests in its capacity to process hypergraphs, transforming the characteristic attributes from urban nodes into hyperedge features. Incorporation of this module allows the dynamic spatial relationships between diverse cities to be efficaciously amalgamated. In cases where the HCM is omitted, the error within the model rises substantially, serving to highlight the critical importance of the HCM in capturing and exploiting the structural relationships among urban nodes. This infers that the HCM is responsible for a contribution of 43% towards overall errors emerging within the STHFM. Simultaneously, the TCM endeavours to process the TRI data, inherently fused with nodal spatial features and COVID-19 data characteristics, thereby encapsulating the temporal dependency features of TRI. Constituted by dilated and causal convolutions, the elimination of this module leads to significant surge in model errors, subtly pointing towards the cruciality of the TCM in discerning alterations in TRI over time. In the grander scheme, the TCM contributes to 33% of the total errors in the STHFM. On the other hand, the DFM employs residual connections to merge hypergraph features and COVID-19 data. This union allows the model to dynamically consolidate features from TRI data and COVID-19 data. In the event that the DFM is excluded, the model's performance would be detrimentally impacted, affirming the integral role that this module performs within the overall model. Consequently, DFM's contribution toward the collective error of the STHFM amounts to 24%. In summary, by integrating the HCM, TCM, and DFM, the model successfully mitigates prediction errors, thereby enhancing prediction effect. Notably, despite DFM's comparatively smaller margin of improvement, the HCM and TCM hold superior value in amplifying the model's effect, with DFM's contribution holding substantial significance.

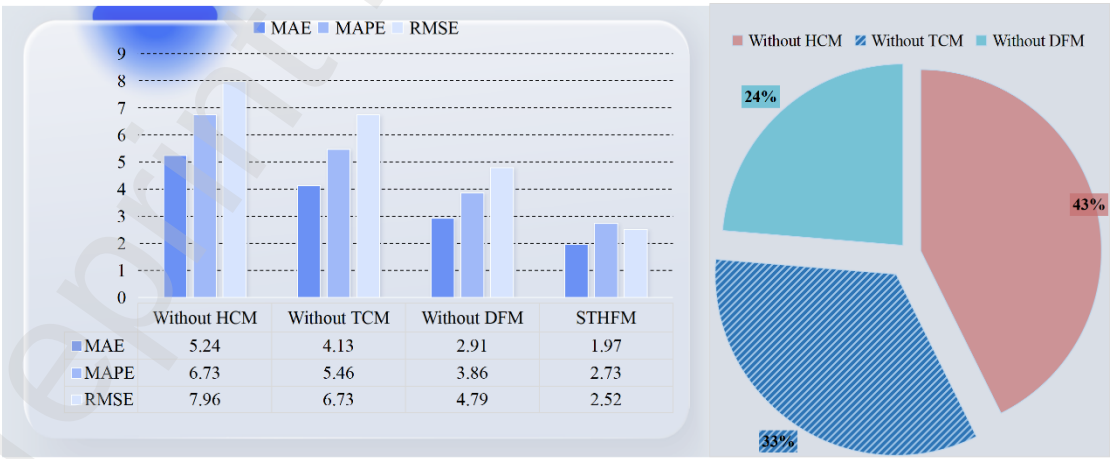

	Without HCM	Without TCM	Without DFM	STHFM
MAE	5.24	4.13	2.91	1.97
MAPE	6.73	5.46	3.86	2.73
RMSE	7.96	6.73	4.79	2.52

Figure 13. The results of the ablation experiments of STHFM. The HCM represents hypergraph convolution module. The TCM represents temporal convolution module. The DFM represents data fusion module.

6 Conclusion

The TRI provides an illuminating snapshot of urban traffic recovery under the constraints of the COVID-19 pandemic, offering valuable insights pertinent to traffic management, public safety, and economic revival, all of which hold enormous significance for governmental bodies and policymakers. Graph models, robust tools hitherto in capturing and predicting TRI dynamics, utilize graphs to elucidate traffic connections amongst cities, presenting not merely the state of traffic flows, but unmasking the intricacy of spatial relations and typographical characteristics of urban traffic networks. Nevertheless, traditional graph models grapple with intricate interactions such as multiple-city traffic routes, typically reducing them to interconnected segments. In light of this predicament, this study postulates the use of hypergraph as an alternative to traditional graph models. Notable for its capability to connect multiple nodes via a single edge, the hypergraph intuitively delineates complex intercity traffic routes and conveys the connectedness amongst cities from a higher perspective, playing an essential role in understanding the vitality of traffic recovery under the COVID-19 pandemic. Taking these factors into consideration, a novel model framework called the STHFM has been introduced, which integrates a hypergraph convolution module capturing spatial features of cities, a temporal convolution module unearthing TRI sequential attributes, and a data fusion module assimilating COVID-19 related data. Compared to existing models, the STHFM excels in long-term TRI forecasting, thereby reducing composite predictive errors by 51.66%.

While this study yields fruitful results in TRI long-term forecasting, challenges remain on the horizon. Foremost is the dependency of the STHFM on input data quality while absorbing and integrating TRI with COVID-19 data. More specifically, if the input data are beset with quality issues or lack comprehensive detail (such as incomplete or missing traffic data from certain cities), the ultimate predictive results could be skewed. Consequently, the STHFM warrants further enhancement to effectively deal with sparse data. Furthermore, the process of employing a hypergraph to comprehend intricate connections and multiple interactions amongst cities could inflict substantial computational burden. Despite its capability to delve into complex problems, its computational complexity might inhibit the model's applicability when managing large-scale problems or conducting real-time data analysis. Although the STHFM exhibits remarkable performance in predicting urban traffic recovery under the influence of COVID-19, expectations stand that similar excellence would be maintained when addressing other types of problems. However, such an assumption necessitates further empirical validation. The direction for future progress ought to focus on designing methodology that accommodates sparse data input and processing, optimizing the model to diminish computational complexity, and trial under diversified scenarios to authenticate the model's broad applicability.

Conflicts of Interests

The authors declare that they have no known competing financial interests or personal relationships that could have appeared to influence the work reported in this study.

Acknowledgement

This research was supported in part by National Natural Science Foundation of China Joint Fund Key Project under Grant No. U22B2057.

References

[1] Hussain A, Mandić A, Fusté-Forné F. Transforming communities: Analyzing the effects of infrastructure and tourism development on social capital, livelihoods, and resilience in Gilgit-Baltistan, Pakistan[J]. Journal of Hospitality and Tourism Management, 2024, 59: 276-295.

[2] Gupta J, Khobragade V J, Upadhyay R K. Enhancing Multimodal Transportation in India: Jogighopa Multimodal Logistics Park[M]//Intelligent Transportation System and Advanced Technology. Singapore: Springer Nature Singapore, 2024: 123-157.

[3] Turan B, Hemmelmayr V, Larsen A, et al. Transition towards sustainable mobility: the role of transport optimization[J]. Central European Journal of Operations Research, 2024, 32(2): 435-456.

[4] Hassanpour A, Bigazzi A. Operating speed distributions in off-street cycling facilities by vehicle type and motorization[J]. Journal of Cycling and Micromobility Research, 2024, 2: 100021.

[5] Zhang S, McGhee D. Towards a Notion of Relational Sacrifices: Nursing During the COVID-19 Pandemic in Wuhan[J]. Ethics and Social Welfare, 2024: 1-15.

[6] BV S K, Fedujwar R, Agarwal A. Travel Time Variability of Bus Routes in Delhi Using Real-Time GTFS Data[C]//2024 16th International Conference on COMmunication Systems & NETworkS (COMSNETS). IEEE, 2024: 210-215.

[7] Wang S, Li Z, Wei H, et al. Revealing inherent interrelationships of direct and indirect factors impacting Driver's stop-or-go behaviors at Yellow-Light[J]. Transportation research part F: traffic psychology and behaviour, 2024, 102: 294-315.

[8] Li X, Li X, Shi J. Capacity sharing for ride-sourcing platforms under competition[J]. Transportation Research Part E: Logistics and Transportation Review, 2024, 182: 103397.

[9] Vighi F. 6 COVID-19 and the emergency loop of implosive capitalism[J]. COVID-19 and the Left: The Tyranny of Fear, 2024: 47.

[10] Rishi N, Sharma V, Gupta D D, et al. Crisis-driven innovations in marketing[J]. Industrial Marketing Management, 2024, 119: 135-146.

[11] Suder M, Gurgul H, Barbosa B, et al. Effectiveness of ATM withdrawal forecasting methods under different market conditions[J]. Technological Forecasting and Social Change, 2024, 200: 123089.

[12] Zhang X, Yang Q, Xu X, et al. Have mixed traffic restrictions improved air quality in different regions? [J]. Transport Policy, 2024, 150: 139-148.

[13] Ray A. Coping with crisis and precarity in the gig economy:'Digitally organised informality', migration and socio-spatial networks among platform drivers in India[J]. Environment and Planning A: Economy and Space, 2024: 0308518X231220296.

[14] Wang F, Li S, Liu L, et al. A novel index for assessing the rural population hollowing at fine spatial resolutions based on Tencent social media big data: A case study in Guangdong Province, China[J]. Land Use Policy, 2024, 137: 107028.

[15] Zhang M, Cheng R, Fei J, et al. Enhancing Digital Innovation Ecosystem Resilience through the Interplay of Organizational, Technological, and Environmental Factors: A Study of 31 Provinces in China Using NCA and fsQCA[J]. Sustainability, 2024, 16(5): 1946.

[16] Zhao J, Li X, Chen L, et al. Scenario analysis of the eco-efficiency for municipal solid waste management: A case study of 211 cities in western China[J]. Science of The Total Environment, 2024, 919: 170536.

[17] Zhao T, Zhang G. Enhancing Major Depressive Disorder Diagnosis with Dynamic-Static Fusion Graph Neural Networks[J]. IEEE Journal of Biomedical and Health Informatics, 2024.

[18] Chen W, Yang K, Yu Z, et al. A survey on imbalanced learning: latest research, applications and future directions[J]. Artificial Intelligence Review, 2024, 57(6): 1-51.

[19] Liu X, Feng H, Wu J, et al. Computing hypergraph homology[J]. Foundations of Data Science,

2024, 6(2): 172-194.
[20] Zhang N, Ma F, Guo D, et al. A novel hypergraph model for identifying and prioritizing personalized drivers in cancer[J]. PLOS Computational Biology, 2024, 20(4): e1012068.
[21] Wang B, Shen Y, Yan X, et al. An autoregressive integrated moving average and long short-term memory (ARIM-LSTM) hybrid model for multi-source epidemic data prediction[J]. PeerJ Computer Science, 2024, 10: e2046.
[22] DR M, El Akmal M, Ula M, et al. Facial-Based Autism Classification Using Support Vector Machine Method[J]. International Journal of Computing and Digital Systems, 2024, 16(1): 875-886.
[23] Zhang Z, Ren S, Qian X, et al. Towards Invariant Time Series Forecasting in Smart Cities[C]//Companion Proceedings of the ACM on Web Conference 2024. 2024: 1344-1350.
[24] Agunwamba J, Tiza M T, Okafor F. An appraisal of statistical and probabilistic models in highway pavements[J]. Turkish Journal of Engineering, 2024, 8(2): 300-329.
[25] Yang H, Li Z, Qi Y. Predicting traffic propagation flow in urban road network with multi-graph convolutional network[J]. Complex & Intelligent Systems, 2024, 10(1): 23-35.
[26] Ma J, Zheng S, Lin S, et al. A City Shared Bike Dispatch Approach Based on Temporal Graph Convolutional Network and Genetic Algorithm[J]. 2024.
[27] Lu Y J, Li C T. Forecasting Urban Sensory Values through Learning Attention-adjusted Graph Spatio-temporal Networks[J]. ACM Transactions on Spatial Algorithms and Systems, 2024, 10(1): 1-22.
[28] Zhang Y, Wang P, Wang B, et al. Adaptive and Interactive Multi-Level Spatio-Temporal Network for Traffic Forecasting[J]. IEEE Transactions on Intelligent Transportation Systems, 2024.
[29] Du S, Yang T, Teng F, et al. Multi-scale feature enhanced spatio-temporal learning for traffic flow forecasting[J]. Knowledge-Based Systems, 2024: 111787.
[30] Lv Z, Li J, Dong C, et al. Deep learning in the COVID-19 epidemic: A deep model for urban traffic revitalization index[J]. Data & Knowledge Engineering, 2021, 135: 101912.
[31] Wang Y, Lv Z, Sheng Z, et al. A deep spatio-temporal meta-learning model for urban traffic revitalization index prediction in the COVID-19 pandemic[J]. Advanced Engineering Informatics, 2022, 53: 101678.
[32] Lv Z, Wang X, Cheng Z, et al. A new approach to COVID-19 data mining: A deep spatial–temporal prediction model based on tree structure for traffic revitalization index[J]. Data & Knowledge Engineering, 2023, 146: 102193.
[33] Lv Z, Ma Z, Xia F, et al. A transportation Revitalization index prediction model based on Spatial-Temporal attention mechanism[J]. Advanced Engineering Informatics, 2024, 61: 102519.
[34] Yadav H, Thakkar A. NOA-LSTM: An efficient LSTM cell architecture for time series forecasting[J]. Expert Systems with Applications, 2024, 238: 122333.
[35] Zhou S, Sun Z, Liu H. D-index and Q-index for spanning trees with leaf degree at most k in graphs[J]. Discrete Mathematics, 2024, 347(5): 113927.
[36] Jin Y, Yin W, Wang H, et al. Capturing word positions does help: A multi-element hypergraph gated attention network for document classification[J]. Expert Systems with Applications, 2024: 124002.
[37] Defferrard M, Bresson X, Vandergheynst P. Convolutional neural networks on graphs with fast localized spectral filtering[J]. Advances in neural information processing systems, 2016, 29.
[38] McDonald T, Tsay C, Schweidtmann A M, et al. Mixed-integer optimisation of graph neural networks for computer-aided molecular design[J]. Computers & Chemical Engineering, 2024, 185: 108660.
[39] Li A, Qiu C, Kloft M, et al. Zero-shot anomaly detection via batch normalization[J]. Advances in Neural Information Processing Systems, 2024, 36.

[40] Omar A, Abd El-Hafeez T. Optimizing epileptic seizure recognition performance with feature scaling and dropout layers[J]. Neural Computing and Applications, 2024, 36(6): 2835-2852.
[41] Dai N, Lei I M, Li Z, et al. Recent advances in wearable electromechanical sensors—Moving towards machine learning-assisted wearable sensing systems[J]. Nano Energy, 2023, 105: 108041. ting and Applications, 2024, 36(6): 2835-2852.
[42] Malenza G, Cesare V, Aldinucci M, et al. Toward HPC application portability via C++ PSTL: the Gaia AVU-GSR code assessment[J]. The Journal of Supercomputing, 2024: 1-22.
[43] Sun X, Zhang T, Sun J, et al. The seroepidemiology of immunoglobulin G antibodies against pertussis toxin and filamentous hemagglutinin in the east of China during the COVID-19 pandemic[J]. Human Vaccines & Immunotherapeutics, 2024, 20(1): 2331438.
[44] Plante J F, Radatz M. On the Capability of Classification Trees and Random Forests to Estimate Probabilities[J]. Journal of Statistical Theory and Practice, 2024, 18(2): 25.
[45] Liu W, Mao X, Zhang X, et al. Efficient Sparse Least Absolute Deviation Regression with Differential Privacy[J]. IEEE Transactions on Information Forensics and Security, 2024.
[46] Shende A M, Kadam A D, Pathan M G, et al. Global performance indicator (GPI) approach to predict the steel fiber reinforced concrete strength with error analysis[J]. HBRC Journal, 2024, 20(1): 123-137.
[47] Indira G, Bhavani M, Brinda R, et al. Electricity Load Demand Prediction for Microgrid Energy Management System Using Hybrid Adaptive Barnacle-Mating Optimizer with Artificial Neural Network Algorithm[J]. Energy Technology, 2024: 2301091.
[48] Benko Ľ, Munkova D, Munk M, et al. The use of residual analysis to improve the error rate accuracy of machine translation[J]. Scientific Reports, 2024, 14(1): 9293.
[49] Liao H, Wang C, Li Z, et al. Physics-Informed Trajectory Prediction for Autonomous Driving under Missing Observation[J]. Available at SSRN 4809575, 2024.
[50] Azamjon M, Sattarov O, Na D. Enhanced Bitcoin Price Direction Forecasting with DQN[J]. IEEE Access, 2024.
[51] Sebastianelli A, Spiller D, Carmo R, et al. A reproducible ensemble machine learning approach to forecast dengue outbreaks[J]. Scientific Reports, 2024, 14(1): 3807.
[52] Alrumaih T N I, Alenazi M J F. CGAAD: Centrality-and Graph-Aware Deep Learning Model for Detecting Cyberattacks Targeting Industrial Control Systems in Critical Infrastructure[J]. IEEE Internet of Things Journal, 2024.
[53] Wang L. Multimodal robotic music performance art based on GRU-GoogLeNet model fusing audiovisual perception[J]. Frontiers in Neurorobotics, 2024, 17: 1324831.
[54] Juul J L, Benson A R, Kleinberg J. Hypergraph patterns and collaboration structure[J]. Frontiers in Physics, 2024, 11: 1301994.
[55] Yu D, Guo G, Wang D, et al. Modeling dynamic spatio-temporal correlations and transitions with time window partitioning for traffic flow prediction[J]. Expert Systems with Applications, 2024: 124187.